10A.7 IMPOSING LAND-SURFACE FLUXES AT AN IMMERSED BOUNDARY FOR IMPROVED SIMULATIONS OF ATMOSPHERIC FLOW OVER COMPLEX TERRAIN

Katherine A. Lundquist[1,2,*], Fotini K. Chow [1], Julie K. Lundquist [2], and Jeffery D. Mirocha [2]
[1] University of California, Berkeley, CA
[2] Lawrence Livermore National Laboratory, Livermore, CA

1 INTRODUCTION

Boundary layer flows are greatly complicated by the presence of complex terrain which redirects mean flow and alters the structure of turbulence. Surface fluxes of heat and moisture provide additional forcing which induce secondary flows, or can dominate flow dynamics in cases with weak mean flows. Mesoscale models are increasingly being used for numerical simulations of boundary layer flows over complex terrain. These models typically use a terrain-following coordinate transformation, but these introduce numerical errors over steep terrain. An alternative is to use an immersed boundary method which alleviates errors associated with the coordinate transformation by allowing the terrain to be represented as a surface which arbitrarily passes through a Cartesian grid.

This paper describes coupling atmospheric physics models to an immersed boundary method implemented in the Weather Research and Forecasting (WRF) model in previous work [Lundquist et al., 2007]. When the immersed boundary method is used, boundary conditions must be imposed on the immersed surface for velocity and scalar surface fluxes. Previous algorithms, such as those used by Tseng and Ferziger [2003] and Balaras [2004], impose no-slip boundary conditions on the velocity field at the immersed surface by adding a body force to the Navier-Stokes equations. Flux boundary conditions for the advection-diffusion equation have not been adequately addressed. A new algorithm is developed here which allows scalar surface fluxes to be imposed on the flow solution at an immersed boundary. With this extension of the immersed boundary method, land-surface models can be coupled to the immersed boundary to provide realistic surface forcing. Validation is provided in the context of idealized valley simulations with both specified and parameterized surface fluxes using the WRF code. Applicability to real terrain is illustrated with a fully coupled two-dimensional simulation of the Owens Valley in California.

*Corresponding author address: Katherine A. Lundquist, Mechanical Engineering, 6189 Etcheverry Hall, University of California, Berkeley, 94720-1742, email: katielundquist@berkeley.edu

2 NUMERICAL METHODOLOGY

The solver for the WRF model is described in this section. Details are included for the governing equations, spatial and temporal discretization, and boundary conditions. New boundary condition options have been added to the existing WRF options, and include a no-slip velocity condition and the use of flux boundary conditions provided by physics parameterizations for all of the large-eddy closure options. Following this, the modifications needed to include the effects of the immersed boundary are discussed.

2.1 THE WEATHER RESEARCH AND FORECASTING MODEL

WRF is an open source community model that is designed for a variety of purposes ranging from operational weather forecasting to idealized geophysical flow simulations. Currently there are two dynamics solvers that will operate within the WRF framework. The core known as Advanced Research WRF (ARW) was used for these simulations, and is the focus of the following discussion.

ARW is a conservative finite-difference model that solves the non-hydrostatic compressible Navier-Stokes equations given by the set of equations labeled 1.

$$\partial_t \vec{V} + \vec{V} \cdot \nabla \vec{V} + \alpha \nabla p + \vec{g} = \vec{F} \tag{1a}$$

$$\partial_t \rho + \nabla \cdot (\rho \vec{V}) = 0 \tag{1b}$$

Here α is the specific volume, and $\vec{F}$ includes Coriolis effects and any additional forcing terms such as turbulent mixing or model physics. Additionally, WRF uses a terrain-following hydrostatic pressure

coordinate allowing pressure to replace height as an independent variable. Laprise [1992] developed a transformation of the fully-compressible non-hydrostatic Euler equations into a terrain-following isobaric coordinate, forming the foundation of the governing equations found in WRF.

The vertical pressure or mass coordinate η is given in terms of the dry hydrostatic pressure P_{hs}, and defined such that it is zero at the top of the model, and unity at the surface of the terrain. The mass of the fluid in the column per unit area is then denoted by μ. This yields the coordinate definition $\eta = \frac{P_{hs} - P_{hs\,top}}{\mu}$, where $\mu(x,y) = P_{hs\,surface} - P_{hs\,top}$. Once the transformation to this coordinate system is applied, the strong conservation form of the Navier-Stokes equations takes the form given in 2. For reference, these equations are also given in the NCAR technical note on WRF [Skamarock et al., 2005, Section 2.2], where the notation differs slightly.

$$\partial_t \mu + \nabla \cdot (\mu \vec{V}) + \partial_\eta (\mu \dot{\eta}) = 0 \tag{2a}$$

$$\partial_t (\mu \vec{V}) + \nabla \cdot (\mu \vec{V}; \vec{V}) + \partial_\eta (\mu \dot{\eta} \vec{V}) - \nabla (p \partial_\eta \phi) + \partial_\eta (p \nabla \phi) = \vec{F} \tag{2b}$$

$$\partial_t (\mu w) + \nabla \cdot (\mu \vec{V} w) + \partial_\eta (\mu \dot{\eta} w) - g\,(\partial_\eta p - \mu) = F \tag{2c}$$

In the set of equations above (2) the velocity vector $\vec{V}$ includes the horizontal velocities, and Del operates in the horizontal dimensions. The variable ϕ is the geopotential, and is defined as $\phi = gz$. Additionally the dot notation in $\dot{\eta}$ denotes differentiation with respect to time, and the semicolon notation represents the dyadic product.

In addition to the conservation of mass and momentum, an equation for potential temperature is solved. Potential temperature θ is a conserved quantity when the atmosphere is assumed to be adiabatic, so the governing equation takes the form used for a conserved scalar (3). The scalar equation is also applied to variables representing moisture (such as water vapor q_v and ice q_i) and passive scalars.

$$\partial_t (\mu \varphi) + \nabla \cdot (\mu \vec{V} \varphi) + \partial_\eta (\mu \dot{\eta} \varphi) = F_\varphi \tag{3}$$

Pressure is then diagnosed from the equation of state below, where γ_{dry} is the ratio of heat capacities of dry air C_p/C_v, p_o is the surface pressure, and R_{dry} is the universal gas constant:

$$p = p_o \left(\frac{R_{dry}\theta}{p_o \alpha_{dry}} \right)^{\gamma_{dry}} \tag{4}$$

WRF is spatially discretized using an Arakawa-C staggered grid. Uniform grid spacing is used in the horizontal directions, and the terrain-following grid may be stretched in the vertical direction. A time split integration scheme is used to deal with the full range of frequencies admitted by the compressible Navier-Stokes equations. In this scheme a third order explicit Runge-Kutta method is used for time advancement of meterologically significant low frequency physical modes, while a smaller time step is needed to account for the higher frequency modes such as acoustic waves. Horizontally propagating acoustic modes are integrated using an explicit forward-backward scheme, and vertically propagating acoustic modes and buoyancy oscillations are treated implicitly.

Several options for lateral boundary conditions are available for use in WRF. These are detailed in Skamarock et al. [2005] and include periodic, open or radiative, symmetric, and specified. In the vertical direction, the top boundary condition is specified to be isobaric, and the Cartesian vertical velocity w is set to zero. Additionally, gravity waves can be absorbed with a diffusive or Rayleigh damping layer. At the bottom boundary the contravariant coordinate velocity is set to zero, and a kinematic boundary condition is used for the Cartesian vertical velocity. The set of equations given by 5a and 5b create a free slip bottom boundary condition.

$$\dot{\eta}_{surf} = 0 \tag{5a}$$

$$w_{surf} = \vec{V} \cdot \nabla h \tag{5b}$$

In equation 5b, h is a function specifying the terrain height. The horizontal velocities used in this equation are extrapolated to the surface using a quadratic Lagrange polynomial. The shear stress at the boundary is implicitly set to zero, unless the effects of friction are taken into account by using log-law similarity theory. At the bottom boundary horizontal gradients of scalars are zero. The vertical gradients are zero unless forcing is provided by a parameterization.

$$\nabla \varphi = 0 \tag{6a}$$

$$\partial_\eta \varphi = f \tag{6b}$$

A no-slip bottom boundary condition has been added to WRF as an additional option beyond the

standard boundary conditions available in the code. In order to add this option, several modifications were made to the original WRF boundary conditions. These changes are detailed in Lundquist et al. [2007]. When the no-slip option is used, the first velocity boundary condition (5a) is still appropriate, as it sets the contravariant velocity of the bottom coordinate to zero. This ensures that the bottom coordinate follows the terrain, and does not change position in time. The kinematic boundary condition given by 5b is no longer valid, and is replaced with the requirement that the Cartesian vertical velocity $w = 0$ on the boundary. The need to extrapolate the horizontal velocities to the surface is eliminated, therefore no approximations are made in our formulation of the no-slip boundary condition. With these changes, the no-slip boundary condition is satisfied for the advective fluxes in the continuity and momentum equations. If turbulent mixing is included in the model, then additional boundary conditions must be imposed on the diffusive flux terms in the momentum equation in order to achieve a no-slip condition. WRF employs eddy viscosity type turbulence models so that the stress tensor is given by 7.

$$\tau_{ij} = -\mu\nu_t D_{ij} \tag{7}$$

The variable μ is the column mass per unit area, ν_t is the turbulent eddy viscosity, and D_{ij} is twice the strain rate or deformation tensor. The calculation of the deformation tensor is modified to include the effects of the no slip boundary condition. In the native WRF boundary condition deformation is zero on the surface. For the no-slip boundary condition, the surface values are calculated, and the new values of the deformation tensor are used for calculating the turbulent stresses.

2.2 FORCING AND RECONSTRUCTION AT THE IMMERSED BOUNDARY

Immersed boundary method (IBM) functionality has been added to the Weather Research and Forecasting model through modification to the source code and the addition of a FORTRAN module. The implementation of the immersed boundary method for the no-slip boundary condition was described in previous work [Lundquist et al., 2007], where forcing was added to the momentum equation. The method used for imposing scalar fluxes in the advection-diffusion equation is described here.

IBM is a technique used to represent the effects of solid boundaries on a non-conforming structured grid. The effects of the external forcing of the fluid by the boundaries are represented by the addition of a force term F_B in the advection-diffusion equation for scalars (8). The forcing term takes a non-zero value at computational nodes in the vicinity of the immersed boundary, but has no effect away from the boundaries.

$$\partial_t\varphi + \vec{V}\cdot\nabla\varphi = \nu_t\nabla^2\varphi + F_\varphi + F_B \tag{8}$$

Treatment of the forcing term has varied among researchers since IBM was introduced by Peskin in 1972. The method used in this work falls into a category commonly referred to as discrete or direct forcing which first appeared in Mohd-Yusof [1997], and was subsequently used by Fadlun et al. [2000], Iaccarino and Verzicco [2003], and others.

In the case that the boundary is coincident with computational nodes, it is clear that the boundary condition can be imposed by assigning it at the coincident node. However when the boundary passes through the grid in an arbitrary manner, the discrete grid points are not generally aligned with the boundary. In particular this is the case on staggered grids, like the one used in WRF. An interpolation method must be used to determine the forcing needed at actual computational nodes; this procedure is often called boundary reconstruction.

The first step in boundary reconstruction is to specify the terrain independently of the grid. For the implementation into the WRF model we have allowed specification of terrain height at twice the resolution of the grid. Specifying the terrain elevation in the $x - y$ plane is consistent with the typical format of digital elevation data.

The next step is the determination of cells that are cut by the immersed boundary. With a staggered grid, cut cells must be determined for each flow variable that will have a boundary condition imposed. Each node for each variable (u,v,w,θ,q_v,etc.) is marked as interior (solid nodes) or exterior (fluid nodes) to the terrain to define the cut cells. Flow variables such as velocity can be reconstructed at fluid nodes as in Fadlun et al. [2000], or at solid nodes as in Mohd-Yusof [1997]. In this work the velocity is reconstructed at solid nodes. This reconstruction technique is called a ghost cell method, and has been used for incompressible flows by Majumdar et al. [2001], Tseng and Ferziger [2003], and others. Ghost points (depicted in Figure 1) are identified as the layer of nodes belonging to cut cells that are within the interior or solid region of the domain.

The value of the variable at the ghost cell which will enforce the boundary condition (9) must be

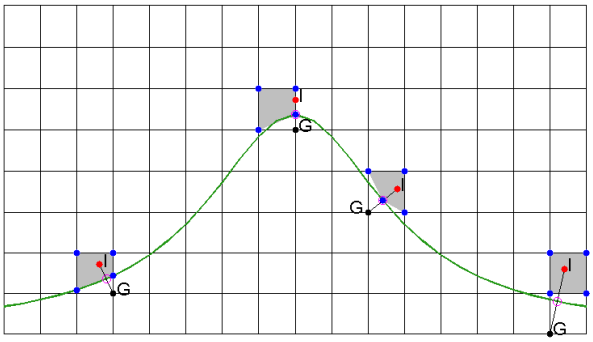

Figure 1: Illustration of the boundary reconstruction method developed for use in WRF. Black ghost points and red image points are labeled with a 'G' and 'I' respectively. Open magenta circles represent boundary points, and closed blue circles are the nearest neighbors of the image point. The interpolation region bounded by the neighbors is shaded in grey.

computed:

$$\frac{\partial \varphi}{\partial \vec{n}} = \vec{n} \cdot \nabla \varphi \tag{9}$$

Several different interpolation methods have been employed by researchers for the purpose of making this calculation, ranging from linear interpolation to inverse distance weighting schemes [Iaccarino and Verzicco, 2003]. For the scalar equations used in WRF, we have developed a unique bilinear reconstruction scheme for two-dimensional terrain.

The bilinear interpolation method used in this work is illustrated in Figure 1, and the equation for a generic variable φ is given by 10.

$$\varphi = c_1 + c_2 x + c_3 z + c_4 xz \tag{10}$$

When the gradient of the interpolation function is substituted into the boundary condition, equation 11 results.

$$\frac{\partial \varphi}{\partial \vec{n}} = c_2 n_x + c_3 n_z + c_4 (n_z x + n_x z) \tag{11}$$

The location of the ghost point is reflected across the boundary in the surface normal direction, and this is labeled an image point. The four nearest neighbors to the image point are determined, and can be computational nodes or boundary points. The weighting coefficients $\vec{c}$ in equations 10 and 11 are determined by solving a system of equations (12) for each ghost point.

$$\vec{c} = \mathbf{V}^{-1} \vec{\phi} \tag{12}$$

The Vandermonde matrix $\mathbf{V}$ contains the locations of the nearest neighbors as they are used in equations 10 and 11. Examples of the choices made are shown in Figure 1, but this illustration is not exhaustive. The (x, z) location of the image point is used in equation (10) to determine φ_I. When a Neumann boundary condition is used, the ghost point and image point have the relationship $\varphi_G = \varphi_I - \overline{GI}(\partial\varphi/\partial\vec{n})$. As a last step, the value calculated from this scheme is assigned to the ghost node.

It should be noted that the hydrostatic pressure coordinate in WRF is not time invariant. Therefore, this procedure, starting with the determination of fluid and solid nodes and ending with imposing the boundary condition by assigning values at the ghost point, must be repeated for each iteration of the solver. The computational penalty for repeating these steps has not been prohibitive, however, the authors are investigating ways to improve efficiency. The simulations presented in section 4 are a direct comparison between WRF with terrain-following coordinates, and WRF with the immersed boundary method. On average, the simulations using IBM required 30% more computational time when compared to the non-IBM solution. The advantage of IBM, as demonstrated in section 5, is that it can handle highly complex terrain. A quantitative comparison of resources could not be made for the cases where WRF is unable to handle the terrain with its original terrain-following grid. Additionally, although the WRF grid is structured, it is not Cartesian. We found that special care must be exercised in determining the interpolation neighbors by accounting for the horizontal gradients in the vertical coordinate.

3 INCLUSION OF ATMOSPHERIC PARAMETERIZATIONS

The WRF model (version 2.2) is currently designed to characterize vertical mixing with a planetary boundary layer (PBL) scheme. Many of the atmospherics physics schemes are designed to work with specific PBL schemes. For instance, the MM5 surface layer scheme is coupled to the Yonsei University (YSU) PBL scheme, and the Eta surface layer scheme is coupled to the Mellor-Yamada-Janjic (MYJ) PBL scheme. More information on these types of WRF details can be found in the code documentation (Skamarock et al. [2005] and Wang et al. [2008]).

WRF also allows for separate closure schemes to perform large-eddy simulations (LES), which

are becoming increasingly attractive for simulations over complex terrain. Currently the LES type closures are not coupled to the atmospheric physics routines. As our interest lies in performing LES over highly complex terrain using the IBM, the WRF code was modified to include an interface between the physics parameterizations and the LES closures. Additionally, code was written to allow idealized cases to be run with surface physics. Finally, because the surface physics interact with the lowest model level, it was necessary to couple these routines to the immersed boundary when IBM-WRF is being used. A description of this last modification follows. The set of schemes that have been coupled to the immersed boundary are the Rapid Radiative Transfer Model (RRTM) for longwave radiation, the MM5 (Dudhia) model for shortwave radiation, the MM5 surface layer scheme, and the NOAH land-surface model.

3.1 RADIATION MODELS

The radiation schemes currently used in WRF are column models, where each column is treated independently. The terrain is treated as if it is a horizontal plane at each column. This is generally acceptable when the horizontal grid spacing is much larger than the vertical grid spacing, but becomes less desirable at smaller aspect ratios. For this reason, these radiation models are acceptable for some complex terrain, but not others. IBM is used in this work for complex mountainous terrain, with the horizontal resolution chosen to be twice the vertical resolution. IBM can be used for a variety of complex terrains, such as urban terrain [Lundquist et al., 2007], but the radiation models would have limited applicability at that resolution.

The RRTM model uses tables to represent longwave radiation due to gasses in the air and optical cloud depth. Upward longwave radiation is dependent upon surface emissivity. Therefore, in order to couple this model with the immersed boundary method the vertical integration limits must be modified to exclude any portion of the atmosphere below the terrain. This is achieved by modifying the portion of the column passed to the integration routine. Additionally, variables such as temperature, pressure, and grid spacing must be modified in the vicinity of the immersed boundary by interpolating these values onto the surface. Finally, surface values such as skin temperature are needed to calculate emissivity. These must also be interpolated to the immersed boundary.

The MM5 (Dudhia) shortwave model works in a similar fashion to the RRTM model. It computes solar flux with a downward integration, and accounts for scattering, water vapor absorption, and cloud albedo and absorption with look-up tables. Coupling to the immersed boundary was again achieved by modifying the vertical integration limits, and using interpolation at the terrain surface.

3.2 SURFACE PHYSICS

Much of the surface physics in WRF is based on similarity theory. These calculations take vertical gradients into account, with the main goal of providing surface fluxes to the vertical diffusion terms as discussed in section 2.1. In cases where the immersed boundary method is used, the fluxes calculated here are applied in a direction normal to the boundary. Imposing the gradient in the normal direction is desirable when the immersed boundary method is used and the terrain slopes are large. The Neumann condition in the normal direction is correct when the flux is specified using a prescribed function, but is less desirable when the flux is calculated by the surface physics routines because these routines use the vertical instead of the normal direction. It is assumed that the atmospheric physics parameterizations included in WRF are not applicable at a scale where this discrepancy would become unacceptable. These parameterizations are applicable to mountainous terrain, and it is shown in section 4 that the use of the normal boundary condition does not create a significant difference in the solution. Thus, while it is possible to impose a vertical gradient with the immersed boundary method, we have chosen to impose a Neumann condition in the normal direction retaining the more rigorous mathematical boundary condition.

The MM5 surface layer is based on Monin-Obukhov similarity theory, and calculates exchange coefficients of heat, moisture, and momentum based on a calculated stability regime. This regime is determined by the bulk Richardson number, defined by 13, where g is the gravitational constant, Z is a reference height above the terrain, Z_{surf} is the surface level, θ_v is virtual potential temperature, and V is the horizontal wind speed which has been modified by a vertical convection velocity.

$$Ri_b = \frac{g(\theta_v(Z) - \theta_v(Z_{surf}))(Z - Z_{surf})}{\theta_v(Z)V(Z)^2} \qquad (13)$$

In the WRF model, the reference height Z is the height of the first grid point above the terrain. When using this equation with the immersed boundary

method, Z is now one point above the ghost point. Therefore, the velocities and temperature, as well as those quantities needed for the conversion to virtual temperature must be modified, along with the reference height. Additionally the surface values must be replaced with values on the immersed boundary. The Monin-Obukhov length scale is then calculated based on the stability class. Next, the 2 m and 10 m reference height data is calculated. Finally, the exchange coefficients are calculated for heat and moisture. Again, the values used in these calculations are modified for the immersed boundary following the example given above for the bulk Richardson number. It is important to note that surface momentum fluxes are not based on Monin-Obukhov theory when the no-slip boundary condition is used, as these conditions are incompatible. This is true of both native WRF, and IBM-WRF.

The NOAH land-surface model is a four layer soil model. It uses radiative and atmospheric forcing from the radiation and surface layer schemes, as well as land-surface properties to provide heat and moisture fluxes. These fluxes serve as the bottom boundary conditions for potential temperature and water vapor. This model also calculates a water budget for the four model layers, including physical effects like evapotranspiration and runoff. Many of the quantities used by the land-surface model have already been modified to include the effects of the immersed boundary by the models discussed above. The NOAH model also makes use of similarity theory. As before, the reference height is set to be one grid point above the immersed boundary or ghost point, and the variables used in the calculation are modified accordingly.

4 IDEALIZED VALLEY SIMULATIONS

In previous work [Lundquist et al., 2007] it was shown that our IBM implementation is able to reproduce results from numerical simulations using the native terrain-following coordinate in WRF. In these simulations, a no-slip boundary condition was imposed on the velocity at the terrain surface and a zero gradient boundary condition was used for potential temperature. These two boundary conditions are adequate for studying a variety of flows, and are commonly the only boundary conditions available in a traditional CFD code. For atmospheric flows it is necessary to represent non-zero fluxes at the surface, such as those of heat and moisture. This section examines the non-zero gradient boundary condition at the immersed terrain in the context of thermally induced slope flows in an idealized valley.

The idealized valley terrain and initialization are identical to that used in the valley winds model intercomparison study [Schmidli et al., 2008], although the resolution used in the following simulations is finer. This case is chosen because the terrain slopes are gentle enough that a direct comparison can be made between WRF using terrain-following coordinates and IBM-WRF. Furthermore, this case is quite challenging for the immersed boundary method. The flow is induced by the approximate boundary conditions at the surface, instead of being induced by a large scale pressure gradient or mean flow.

Both uncoupled and coupled cases are considered. In the uncoupled cases, presented in section 4.1, the surface heating is specified as a function of time. There are no surface or land attributes such as vegetation or soil type. This allows verification of the surface flux condition at the immersed boundary without the added complexity of the land-surface model. In the coupled cases, presented in section 4.2, the surface fluxes are prescribed by atmospheric parameterizations, which have been modified to recognize the immersed boundary as the terrain surface. When the immersed boundary method is coupled with the land-surface model, it not only provides boundary conditions for the atmospheric flow, but it also interacts with the land-surface model.

4.1 SPECIFIED SURFACE FORCING

The test flow case is thermally induced slope flow in a two-dimensional idealized valley. The valley terrain is defined by equation 14, where the peak height is h_p = 1.5 km, the valley floor half-width is V_x = 0.5 km, and the hill half-width is S_x = 9 km.

$$h_t = h_p h_x \tag{14}$$

$$h_x(x) = \begin{cases} 0 \\ if\ |x| \leq V_x \\ 0.5 - 0.5\cos\left(\pi \frac{|x|-V_x}{S_x}\right) \\ if\ V_x < |x| < V_x + S_x \\ 1 \\ if\ V_x + S_x \leq |x| \leq V_x + S_x + P_x \\ 0.5 + 0.5\cos\left(\pi \frac{|x|-(V_x+S_x+P_x)}{S_x}\right) \\ if\ V_x + S_x + P + x < |x| < V_x + 2S_x + P_x \\ 0 \\ if\ |x| \geq V_x + 2S_x + P_x \end{cases}$$

The domain is initialized with a quiescent sounding that is moist and stably stratified. The sounding prescribes a constant 40% relative humidity and the potential temperature is given by equation 15, where θ_s = 280 K, Γ = 3200 K m^{-1}, $\Delta\theta$ = 5 K, and β = 0.002 m^{-1}.

$$\theta(z) = \theta_s + \Gamma z + \Delta\theta\left[1 - \exp(-\beta z)\right] \tag{15}$$

The total domain size is (X, Y, Z) = (60 km, 0.6 km, 10 km) for the WRF simulation with terrain-following coordinates. When IBM-WRF is used, the bottom of the domain is lowered to 200 m below the zero level, so that the domain size is (X, Y, Z) = (60 km, 0.6 km, 10.2 km). This allows a minimum of two grid points below the immersed terrain. In each simulation the horizontal grid spacing is $\Delta X = \Delta Y$ = 200 m. For the WRF simulation the number of grid points used in each direction is (n_x, n_y, n_z) = (301,3,60), and for IBM-WRF it is (n_x, n_y, n_z) = (301,3,62). The vertical grid is not stretched in the pressure coordinate η, however, it is naturally stretched towards the surface in a physical z coordinate. For the terrain-following coordinate, the minimum vertical grid spacing occurs at the mountain peaks and is ΔZ_{min} = 95.6 m. At the domain top the maximum is ΔZ_{max} = 307.8 m. For the IBM-WRF grid with 62 vertical levels, the minimum vertical grid spacing occurs at the bottom level of the domain, which is below the terrain, and is ΔZ_{min} = 101.9 m, At the domain top the maximum is ΔZ_{max} = 307.4 m.

Periodic boundary conditions are used at the lateral boundaries. The top boundary condition is isobaric with no vertical velocity. A diffusive damping layer 3.8 km thick is used at the top of the domain to prevent the reflection of waves. A no-slip boundary condition is used at the terrain surface, and is achieved through the no-slip modifications in the terrain-following WRF or with IBM. Both methods were previously described in section 2. In the uncoupled cases a Neumann boundary condition specified by equation 16 is applied to potential temperature at the terrain.

$$Q(t) = Q_{max}\sin(\omega t) \tag{16}$$

As shown in figure 2 the maximum sensible heat flux is Q_{max} = 200 W m^{-2}. With a period of $\omega = 2\pi/24$ hrs the function represents a daytime heating cycle. Total integration time for the simulation is 12 hours, starting at 6 am and ending at 6 pm (6:00 to 18:00 UTC), with data collected at 15 minute intervals.

A constant eddy viscosity is used in the turbulent diffusion terms. Yasuda [1988] noted that daytime eddy diffusivities typically ranged from 10 to 100 m^2/s. Two sets of results are presented here, the first with an eddy viscosity of 30 m^2/s and the second with 60 m^2/s. These values were chosen to achieve distinct flow properties, as explicitly resolved convective vertical mixing occurs with 30 m^2/s, but not with 60 m^2/s. Figure 3 shows velocity vectors at 15:00 for simulations with the IBM and WRF coordinates with ν_t = 30 m^2/s. Convective cells are well developed at 15:00, and were first visible at 11:45. They have virtually disappeared by the end of the simulation at 18:00.

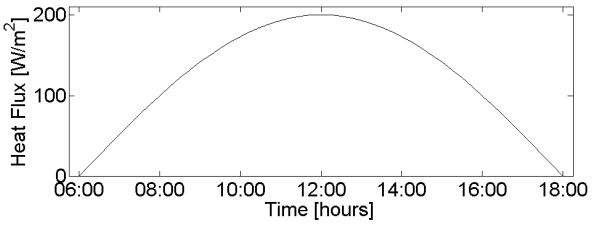

Figure 2: Specified sensible heat flux representing a daytime diurnal cycle.

Figure 4 shows profiles of potential temperature at the valley center as it evolves in time. When comparing the IBM-WRF solution to the WRF solution, IBM under predicts the surface temperature from 6:30 to 8:15, when the two solutions become equal again. At 9:00 the IBM surface temperature becomes higher than in the WRF solution, and remains so for the remainder of the simulation. Slightly unstable conditions are evident near the surface in the profiles at times of 9:00, 12:00, and 15:00. As these plots are instantaneous, and the location of convective cells will vary in each model, exact agreement is not expected. Despite this fact, very good agreement is achieved in the development of the mixed layer between the WRF and IBM-WRF simulations.

When the eddy diffusivity is increased to 60 m^2/s the mixing is strong enough to maintain a neutral stability profile during surface heating, therefore avoiding the formation of thermal convection cells. Figure 5 depicts velocity vectors at 15:00. A clear circulation pattern exists of upslope flow within the valley; the upslope flows converge at the peaks and create a circulation pattern with subsidence at the valley center.

Figure 6 again shows instantaneous potential temperature at the valley center. The evolution of the profiles for the IBM and WRF simulations compare well. Similarly to the previous results, temper-

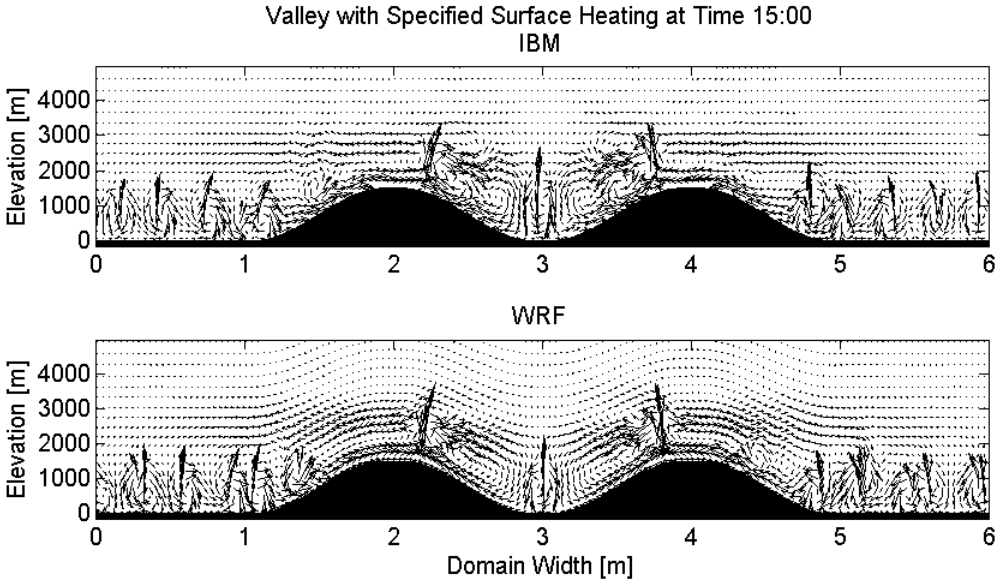

Figure 3: Quiver plots for thermally induced slope flow using IBM-WRF and native WRF. Flow is shown at 15:00 with a constant eddy viscosity of 30 [m^2/s] Every second grid point is shown.

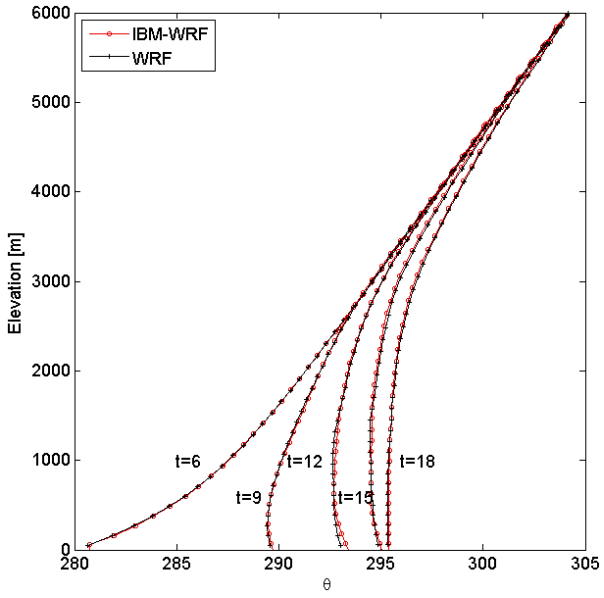

Figure 4: Profiles of potential temperature [K] at the valley center for times 6:00, 9:00, 12:00, 15:00, and 18:00. With an eddy viscosity of 30 [m^2/s] the unstable stratification near the surface creates convective cells.

ature at the surface is slightly less in the IBM simulation than with terrain-following coordinates from 6:30 to 9:30. The surface temperature becomes slightly larger in the IBM simulation at 11:00, and remains larger for the duration of the integration. The overall agreement is excellent.

Although the temperature profiles are equivalent, the velocity profiles and boundary conditions must also be verified. This interaction is best seen in the laminar flow produced with the higher eddy viscosity, and the remainder of this section will focus on analysis of this simulation. Figure 7 includes profiles of u and w velocity at 15:00. The profiles match very well, and show that the no-slip boundary condition at the terrain is achieved. The largest difference in the profiles is observed in the magnitude of the u velocity in the upslope flows. In each of the u profiles the IBM-WRF solution predicts slightly higher velocities in this region. Obvious differences are not present in the profiles of w velocity.

To further analyze the differences between the IBM-WRF and WRF solutions, both time and domain averaged differences are calculated. For this calculation the IBM-WRF solution is interpolated onto the terrain-following WRF grid using a linear interpolation method. In the mass based coordinate system new interpolation constants must be calculated at each time. Once the two solutions are on a common grid they may be compared directly, although the error introduced by the interpolation is unknown. Spatial variations in the two solutions are

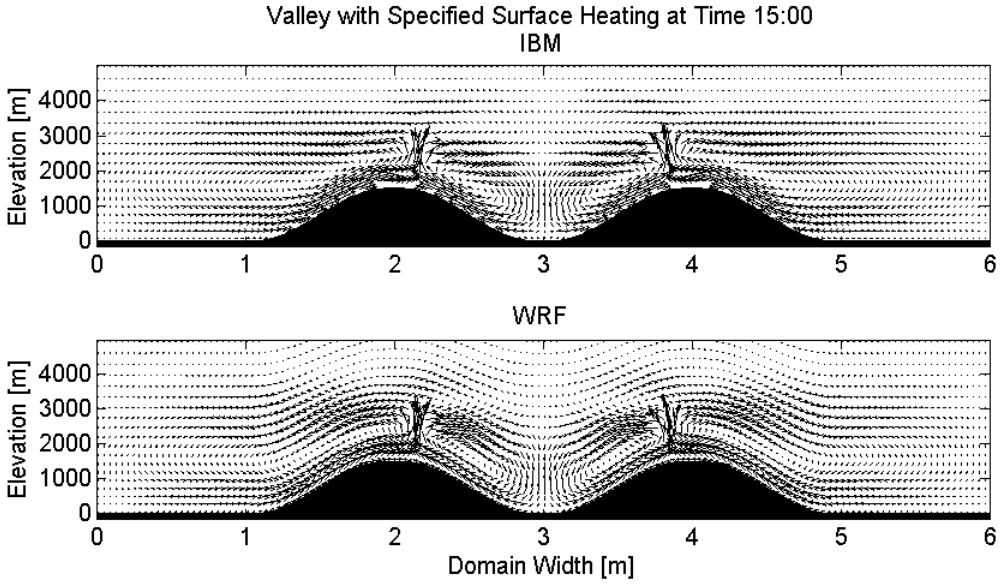

Figure 5: Quiver plots for thermally induced slope flow using IBM-WRF and native WRF. Flow is shown at 15:00 with a constant eddy viscosity of 60 [m^2/s] Every second grid point is shown.

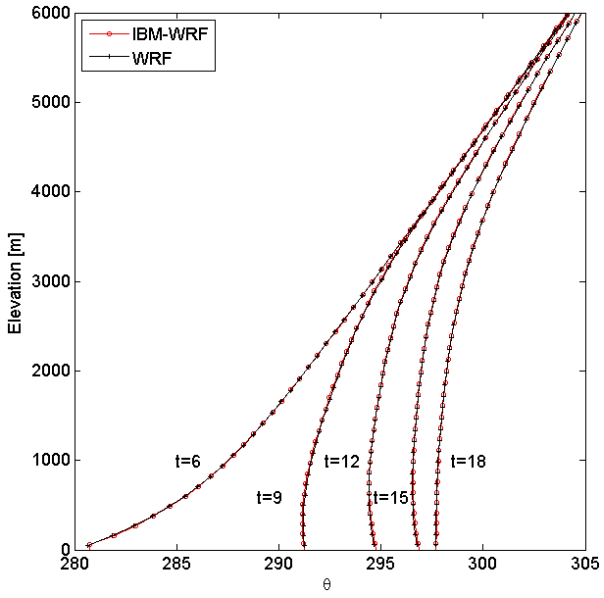

Figure 6: Profiles of potential temperature [K] at the valley center for times 6:00, 9:00, 12:00, 15:00 and 18:00. With an eddy viscosity of 60 [m^2/s] the surface layer is sufficiently mixed so that convective cells do not form.

calculated for a given variable ϕ with equation 17a, and temporal variations are calculated with equation 17b. It is assumed that the grid movement during the simulation is small, so that it may be neglected in the time averaging of equation 17a. Once the spatial difference is calculated, it is plotted on the WRF grid as it is at initialization.

$$\Delta\phi(x,\eta) = \overline{\phi_{IBM}(x,\eta,t) - \phi_{WRF}(x,\eta,t)}^{t} \quad (17a)$$

$$\Delta\phi(t) = \overline{|\phi_{IBM}(x,\eta,t) - \phi_{WRF}(x,\eta,t)|}^{x,\eta} \quad (17b)$$

The results of the time averaged spatial differences are presented in figure 8, which confirms the differences seen in the instantaneous plots. The first figure shows time averaged difference in θ. There is a maximum time averaged difference of $\Delta\theta_{max}$ = 0.0404 K, and a minimum of $\Delta\theta_{min}$ = -0.0333 K between the two simulations. The IBM simulation predicts a higher temperature at the surface with the maximum difference occurring on the valley slopes, and a slightly cooler atmosphere aloft in the valley center. It is unknown what proportion of this difference is attributed to the difference in the boundary conditions as described in section 2, and what is generated by errors in the immersed boundary approximation. These differences in θ contribute to the differences in velocity shown in the next two figures. The velocity differences are ΔU_{max} = ΔU_{min} = $\pm$0.1788 m/s in the u velocity component, and in w they are ΔW_{max} = 0.0507 m/s and ΔW_{min} = -0.0719 m/s. In u the largest

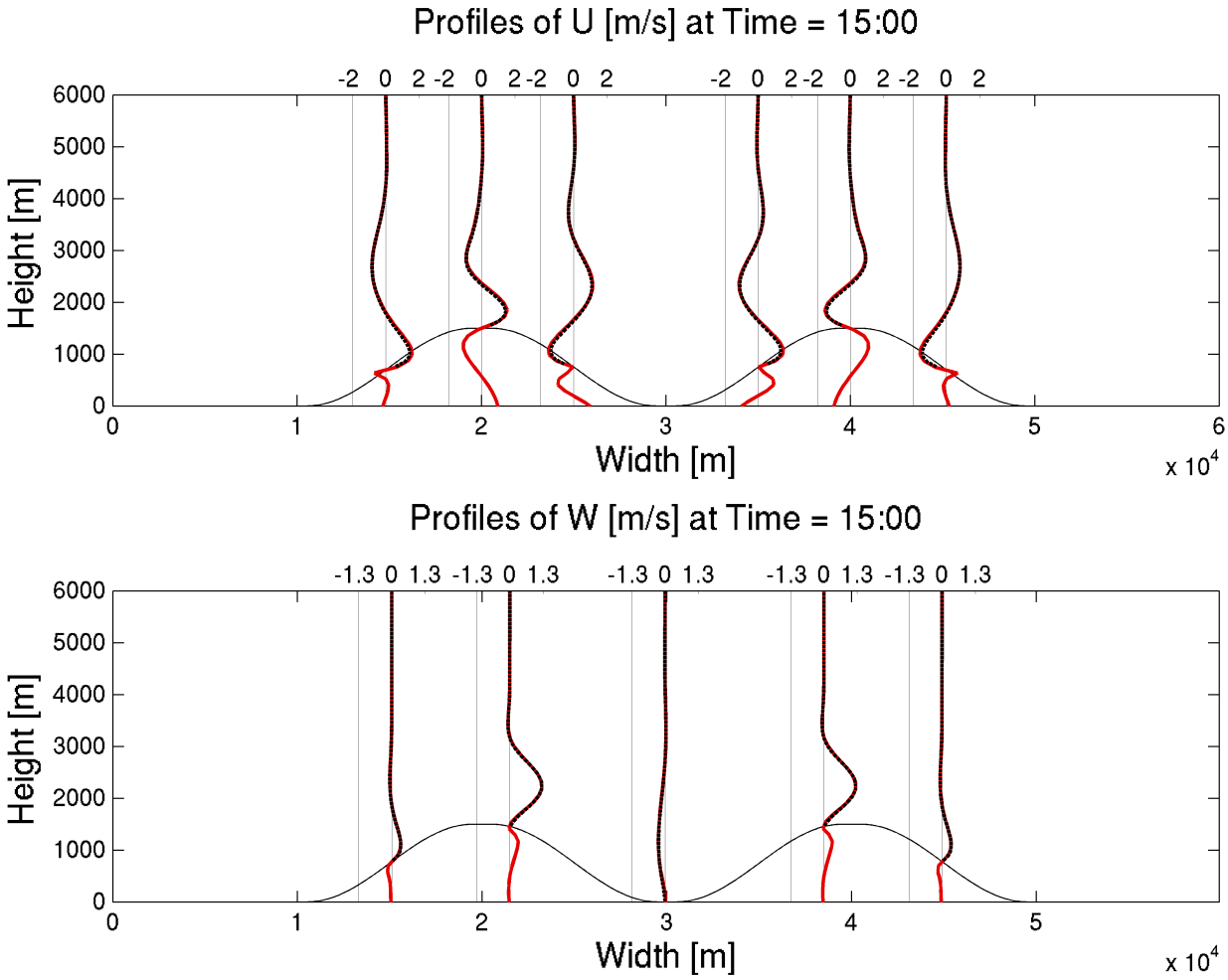

Figure 7: Profiles of u and w velocity for IBM-WRF (show as a solid red line) and WRF with terrain-following coordinates (shown as a black dashed line) at 15:00.

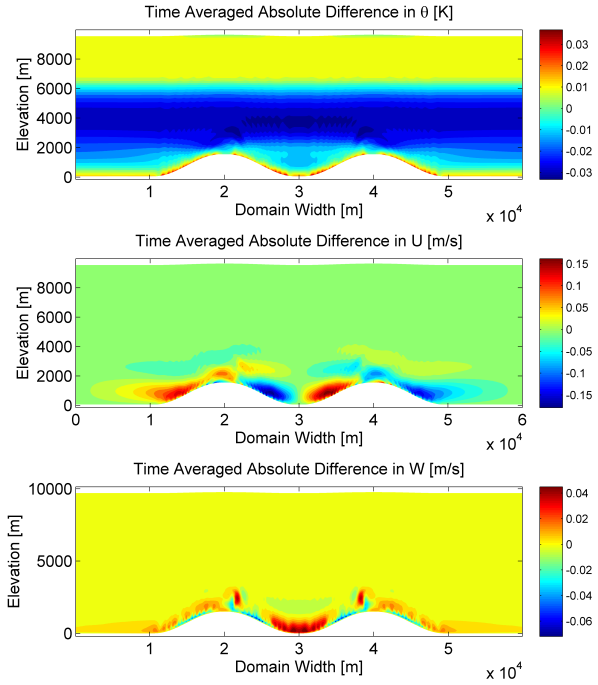

Figure 8: Time averaged spatial differences between independent variables. Potential temperature is plotted first with u and w plotted second and third, respectively. Differences are absolute with units of K for θ, and m/s for velocities.

differences are seen on the valley slopes, specifically inside of the valley. Additionally, differences are seen at the valley center and peaks in w. These differences are relatively small considering that the simulations have different grids and slightly different boundary conditions.

Differences between the simulations can also be viewed as a function of time, as in figure 9. It can be seen here that the potential temperature fields are different at initialization. This is because at initialization the boundary condition is enforced in the IBM simulation, but not in the WRF simulation where the terrain simply intersects the prescribed sounding. Excellent agreement is seen in the potential temperature field, and the differences are smaller at the end of the simulation than they are at initialization. The velocity fields are initialized as quiescent, therefore they are identical at initialization. The differences in velocity peak during the first thirty minutes of the simulation, and then rapidly decrease. A stair step type appearance is observed in the first thirty minutes of the IBM simulation, as the flow adjusts to the immersed boundary. As flow patterns develop, the stepped appearance smooths out and eventually disappears. This peak indicates that differences could be reduced by adding spin-up time to the simulation. It is important to note that the differences do not grow in time, and in fact trend downwards as simulation time increases.

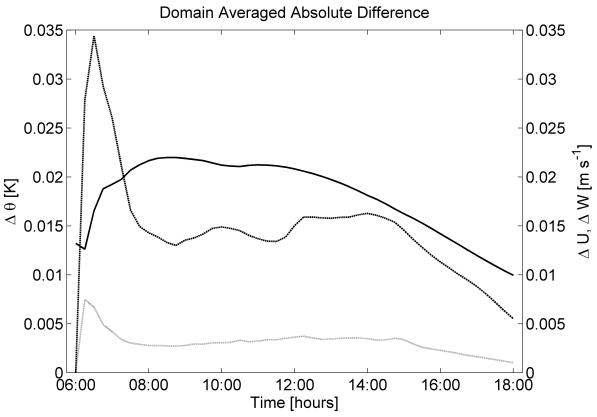

Figure 9: Domain averaged differences as a function of time. Potential temperature is solid, u is dashed, and w is dotted.

4.2 COUPLED SURFACE FORCING

In this section the simulations are fully coupled, meaning that the surface fluxes are calculated by the radiation and land-surface schemes. The domain set-up is as described in section 4.1, however, in this case soil properties are also initialized. The valley is located at 36° North, 0° East. The simulation date is March 21, 2007, and the period is again from 6:00 to 18:00 UTC. Topographic shading in not included in the version of WRF used here (WRFV2.2). The soil is initialized with uniform properties. The soil type is sandy loam, the vegetation type is savannah, and the vegetation fraction is 0.1. The soil temperature is initialized to be in equilibrium with the atmospheric temperature at the surface. Soil moisture is set to a constant volumetric water content of 0.0868 m^3 m^{-3}. Four vertical levels are used in the soil model with depths of 0.1, 0.3, 0.6, and 1 m for a total model depth of 2 m. The Rapid Radiative Transfer Model (RRTM) calculates longwave radiation, and the MM5 (Dudhia) scheme is used to model shortwave radiation. The MM5 surface layer model, which is based on Monin-Obukhov similarity theory, is used along with the NOAH land-surface model. Documentation of these schemes can be found in Skamarock et al. [2005] and the references within. As described in section 3 these schemes have been modified so that they are coupled to the immersed boundary.

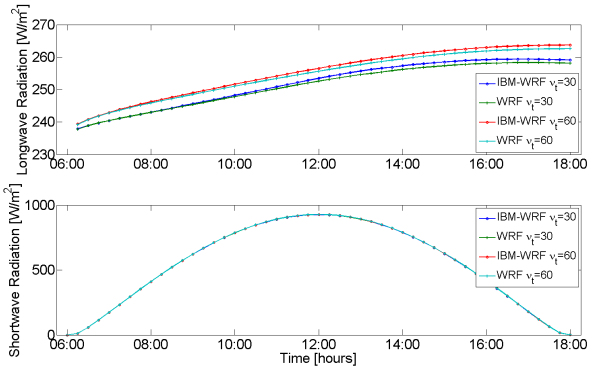

Figure 10: Domain-averaged downward longwave and shortwave radiation for the coupled simulations.

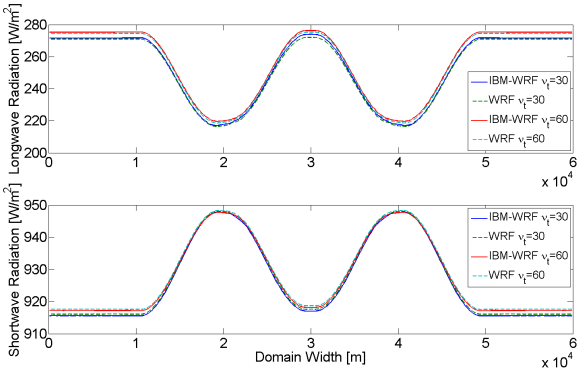

Figure 11: Instantaneous spatial variation in downward longwave and shortwave radiation at 12:00.

As in section 4.1 two sets of simulations were preformed with different turbulent viscosities. The same flow patterns emerged, where convective cells formed at the surface for simulations with ν_t = 30 m^2/s and did not for those with ν_t = 60 m^2/s. It was previously shown that the no-slip and flux boundary conditions are accurate at the immersed boundary, and that they interact properly to produce the correct flows. The focus of this section is to examine the calculation of these fluxes, as well as the inputs needed for these calculations at the immersed boundary.

Longwave and shortwave radiation are inputs to the surface physics schemes. The evolution of domain averaged radiation is plotted in figure 10. Domain averaged longwave radiation varies slightly between the two simulations with different eddy viscosities. The WRF and IBM-WRF cases match almost exactly at the first data point (6:15), but diverge slightly during the simulation. At the end of the simulation (18:00) the difference in longwave radiation is 1.01 W m^{-2} for the lower eddy viscosity, and 1.12 W m^{-2} for the higher eddy viscosity. When normalized by the WRF solution, these are differences of 0.391% and 0.428% respectively. The differences are even smaller for shortwave radiation, where nearly perfect results are achieved.

The spatial variations in longwave and shortwave radiation are documented in figure 11, where they are shown at noon (12:00). There is a difference of about 56 W m^{-2} in longwave radiation from the valley floor to peak. In comparison, at noon there is a maximum difference of 2.0 W m^{-2} in the two simulations at the lower viscosity, and 1.2 W m^{-2} at the higher viscosity. This shows that any error created by coupling the radiation scheme to the immersed boundary is negligible in comparison to variations due to terrain height. Shortwave radiation varies by about 32 W m^{-2} from valley peak to trough. The maximum differences seen here are 0.65 and 0.58 W m^{-2}.

The same types of plots are included for heat and moisture fluxes at the surface, as calculated by the land-surface model. Domain averaged heat and moisture fluxes are plotted in figure 12. It can be seen that heat flux diverges more in the ν_t = 30 m^2/s simulations than in the ν_t = 60 m^2/s simulations. In the simulations with lower eddy viscosity, the peak domain averaged heat flux occurs at 12:45. In the IBM-WRF simulation this peak is 227.9 W m^{-2}, and in the WRF simulation it is 239.3 W m^{-2}. The maximum difference between the two simulations occurs earlier in the day at 12:15, and is a difference of 12.25 W m^{-2}. When normalized by the WRF solution, this is a difference of 5.4%. In the simulations with a higher eddy viscosity the maximum difference between the solutions occurs later in the day at 15:15. The difference at that time is 2.95 W m^{-2} or 2.2%.

Differences in moisture fluxes are much smaller than those seen in heat fluxes. The maximum mean difference in the ν_t = 30 m^2/s simulations occurs at 13:30, and is 4.27e-8 kg m^{-2} s^{-1} in magnitude, which is 0.68% of the WRF value. The maximum mean difference in the ν_t = 60 m^2/s simulations occurs at 9:45, and is 3.18e-8 kg m^{-2} s^{-1} in magnitude, which is 0.74% of the WRF value.

Figure 13 shows the spatial variation in the heat and moisture fluxes at three different times (9:00, 12:00, 15:00) for the simulation with higher eddy viscosity. It is obvious that the spatial variation in the IBM-WRF simulation is much higher than in the terrain-following WRF simulation, although the values are similar when averaged. The exact cause of this variation, along with methods for reducing it are

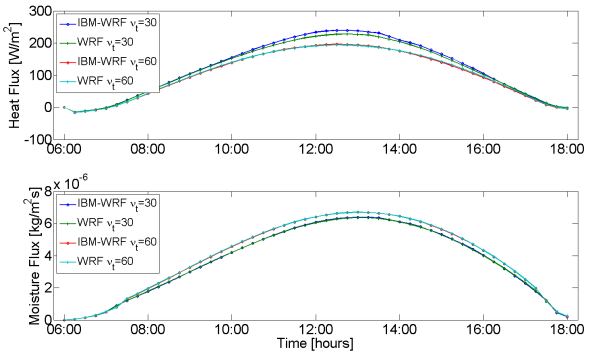

Figure 12: Domain averaged upward heat and moisture flux for the coupled simulations.

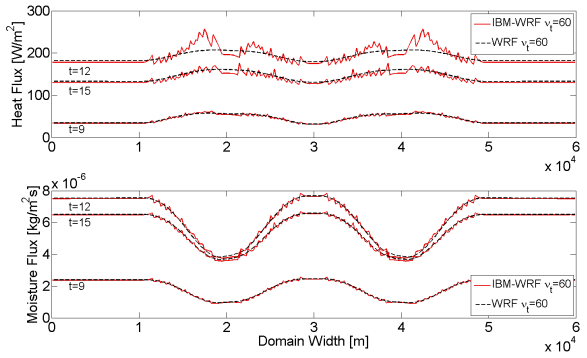

Figure 13: Spatial variation in upward heat and moisture flux at 9:00, 12:00, and 15:00.

under investigation.

Volumetric soil moisture is calculated by the land-surface model. Land-surface models can be used independently of atmospheric simulations, but when coupled the top boundary conditions of the land-surface model are set with inputs from the atmosphere. When IBM is used, it provides boundary conditions to each model (WRF and NOAH) simultaneously. A comparison of soil moisture is shown in Figure 14 for the IBM-WRF and WRF simulations with a 60 m^2/s eddy viscosity. At initialization the soil moisture has a constant volumetric water content of 0.0868 m^3 m^{-3}. During the simulation the soil begins to dry as moisture is transfered to the atmosphere. The depth to which this occurs is affected by the terrain height, and it can be seen that the soil remains slightly more moist at the terrain peaks in comparison to the valley floor and the terrain outside of the valley. Similar results are achieved in both of the simulations.

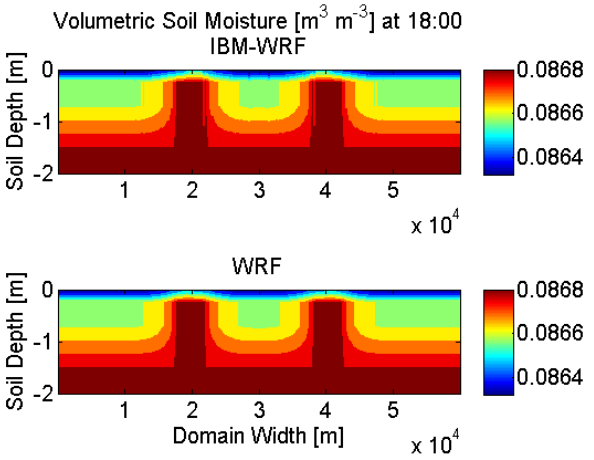

Figure 14: Volumetric soil moisture at the end of the simulation (18:00). This field was initialized with a constant saturation rate.

5 OWENS VALLEY SIMULATIONS

The IBM allows explicit resolution of steep terrain, enabling WRF to simulate flows which cannot be computed using a standard terrain-following coordinate. To demonstrate this capability, we have modeled flow over a two-dimensional slice of the Owens Valley in California. The terrain slice, seen in figure 16, is perpendicular to the valley axis. The terrain data is from the National Elevation Dataset (NED) at a resolution of 1/3 arc-second or approximately 10 m. As the terrain slice is not aligned with latitudinal coordinates, it was necessary to interpolate the data onto the grid. After the interpolation, the terrain resolution used in the simulation is 20 m. As a rule of thumb, terrain-following coordinates should not be used for slopes over 30 degrees. The slope of the 20 m terrain data is plotted in figure 15, and it can be seen that there are several slopes of 60 degrees in this valley profile.

The domain size is (X, Y, Z) = (58.32 km, 0.04 km, 10 km) with (n_x, n_y, n_z) = (1459,2,120) grid points. The grid spacing is ΔX = ΔY = 40 m in the horizontal. The minimum grid spacing in the vertical is ΔZ_{min} = 49.0 m, and the maximum is ΔZ_{max} = 130.6 m. The initialization is the same as in the fully coupled cases in section 4.2, and as in those cases the soil properties are idealized.

Figures 16 and 17 are examples of flows in the Owens Valley. Figure 16 shows a typical morning upslope flow due to diurnal heating. Figure 17 shows westerly flow over the Sierra Nevada mountain range. Mountain waves are seen over the valley.

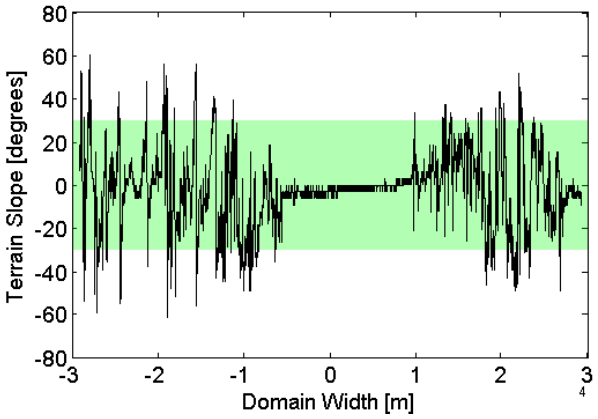

Figure 15: Slope of the Owens Valley terrain data is plotted with the black line. The green background depicts the typical limits of terrain-following coordinates.

6 CONCLUSIONS

This work has demonstrated that the immersed boundary method is a viable option for removing the barriers to modeling complex geometries created by the use of terrain-following coordinates. A new IBM suitable for viscous compressible flows has been developed and implemented in WRF. The IBM produces correct results for both the no-slip velocity and scalar flux boundary conditions. Additionally, the IBM works with atmospheric parameterizations which provide realistic surface forcing. Excellent agreement was achieved for two-dimensional valley flows between the solution calculated on a terrain-following grid and the solution with the immersed boundary. Applicability to realistic, highly-complex mountainous terrain was demonstrated by modeling flow over a 2D slice of the Owens Valley in California. Future work will extend these results to three dimensions, ultimately allowing for seamless grid nesting between mesoscale domains with terrain-following coordinates and highly resolved domains using the immersed boundary method.

7 ACKNOWLEDGEMENTS

The authors would like to thank Hoyt Walker for assistance with the NED terrain data. The first author is grateful for the support of a Lawrence Scholars Program Fellowship from Lawrence Livermore National Laboratory (LLNL). This project was partially funded by the LLNL Laboratory-Driven Research and Development program. The support of National Science Foundation Grant ATM-0645784 [FKC] (Physical Meteorology Program: S. Nelson, Program Director) is also gratefully acknowledged. This work was performed under the auspices of the U.S. Department of Energy by Lawrence Livermore National Laboratory under Contract DE-AC52-07NA27344.

REFERENCES

E. Balaras. Modeling complex boundaries using an external force field on fixed cartesian grid in large-eddy simulations. *Comput. Fluids*, 33:375–404, 2004.

E.A. Fadlun, R. Verzicco, P. Orlandi, and J. Mohd-Yusof. Combined immersed-boundary finite-difference methods for three-dimensional complex flow simulations. *J. Comp. Phys.*, 161:35–60, 2000.

G. Iaccarino and R. Verzicco. Immersed boundary technique for turbulent flow simulations. *Appl. Mech. Rev.*, 56(3): 331–347, May 2003.

R. Laprise. The euler equations of motion with hydrostatic pressure as an independent variable. *Mon. Weather Rev.*, 120(7):197–207, July 1992.

K.A. Lundquist, F.K. Chow, J.K. Lundquist, and J.D. Mirocha. Development of an immersed boundary method to resolve complex terrain in the weather research and forecasting model. In *7th Symposium on the Urban Environment*. American Meteorological Society, 2007.

S. Majumdar, G. Iaccarino, and P. Durbin. RANS solvers with adaptive structured boundary non-conforming grids. Technical report, Center for Turbulence Research, NASA Ames/Stanford Univ., Palo Alto, CA, 2001.

J. Mohd-Yusof. Combined immersed boundary/b-spline methods for simulations of flow in complex geometry. Technical report, Center for Turbulence Research, NASA Ames/Stanford Univ., Palo Alto, CA, 1997.

C.S. Peskin. Flow patterns around heart valves: A numerical method. *J. Comp. Phys.*, 10(2):252–271, October 1972.

J. Schmidli, B.J. Billings, R. Burton, F.K. Chow, S.F.J. DeWekker, J.D. Doyle, V. Grubisic, T.R. Holt, Q. Jiang, K.A. Lundquist, A.N. Ross, L.C. Savage, P. Sheridan, S. Vosper, C.D. Whiteman, A.A.Wyszogrodzki, G. Zaengl, and S. Zhong. The T-REX valley wind model intercomparison project. In *13th Conference on Mountain Meteorology*. American Meteorological Society, 2008.

W.C. Skamarock, J.B. Klemp, J. Dudhia, D.O. Gill, D.M. Barker, W. Wang, and J.G. Powers. A description of the advanced research WRF version 2. Technical Report NCAR/TN-468+STR, National Center for Atmospheric Research, Boulder, CO, June 2005.

Y. Tseng and J.H. Ferziger. A ghost-cell immersed boundary method for flow in complex geometry. *J. Comp. Phys.*, 192:593–623, 2003.

W. Wang, D. Barker, J.Bray, C. Bruyere, M. Duda, J. Dudhia, D. Gill, and J. Michalakes. Arw version 2 modeling system user's guide. Technical report, National Center for Atmospheric Research, Boulder, CO, January 2008.

N. Yasuda. Turbulent diffusivity and diurnal variation in the atmospheric boundary layer. *Boundary-Layer Meteorol.*, 43:209–221, 1988.

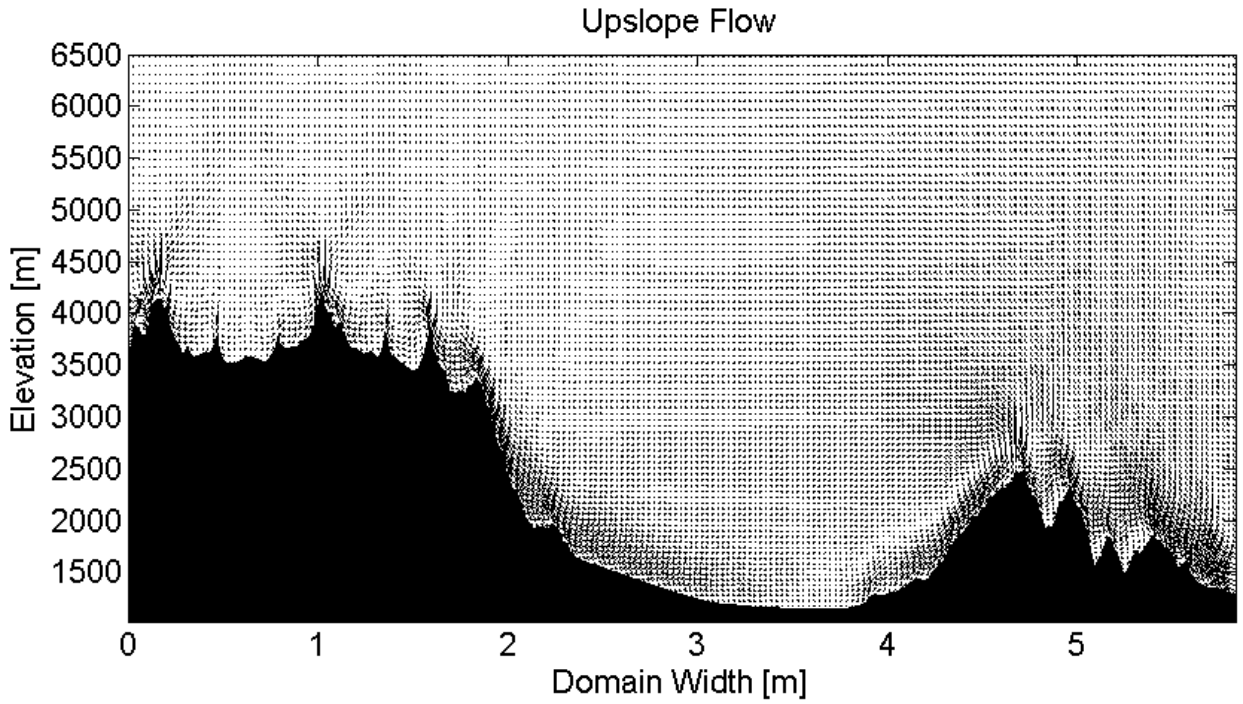

Figure 16: Upslope flow induced by diurnal heating.

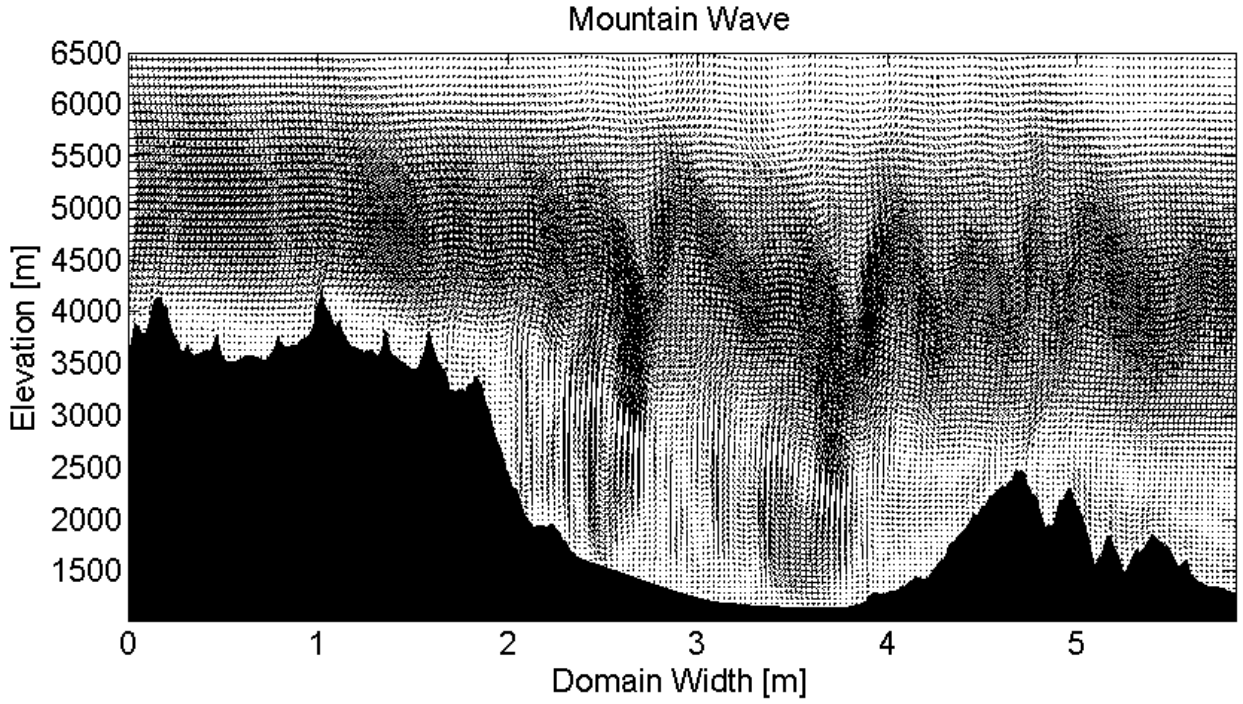

Figure 17: Mountain wave over the Owens Valley from westerly flow over the Sierra Nevada mountain range.